# RAMAN SCATTERING OF CARBON NANOTUBES

H. KUZMANY*

M. HULMAN

R. PFEIFFER

F. SIMON

*Fakultät für Physik der Universität Wien, Wien, A*

Abstract: The present state of Raman scattering from carbon nanotubes is reviewed. In the first part of the presentation the basic concepts of Raman scattering are elucidated with particular emphasis on resonance scattering. The classical and the quantum-mechanical description are presented and the basic experimental instrumentation and procedures are described. Special Raman techniques are discussed. Eventually, a short review on the electronic structure of single wall carbon nanotubes (SWCNTs) is given.

The second part of the presentation deals with Raman scattering from SWCNTs. A group theoretical analysis and the origin of the basic Raman lines are described. For the radial breathing mode the observed quantum oscillations and the unusual strong Raman cross section are discussed. For the G line the resonance behavior and the response to doping is demonstrated and the calculated dependence of the line frequency on the tube diameter is summarized. For the D-line and for the G'- line the dispersion is demonstrated and its origin from a triple resonance is described. Finally, the response from pristine and doped peapods is elucidated.

In the third part most recent results are reported from Raman spectroscopy of double wall carbon nanotubes (DWCNTs). The unusual narrow lines with widths down to 0.4 $cm^{-1}$ indicate clean room conditions for the growth process of the inner tubes. (n,m) assignment to them and high curvature effects are discussed. Results for DWCNTs where the inner tubes are highly $^{13}C$ substituted are reported with respect to Raman and NMR spectroscopy. Eventually, it is demonstrated that the RBM Raman lines of the inner tubes cluster into groups of up to 14 lines where each member of the cluster represents a pair of inner-outer tubes.

Keywords: Raman scattering, single wall carbon nanotubes, peapods, double wall carbon nanotubes, nano clean room, isotope effects



*Journal Information*

Preface

Raman scattering has developed into one of the key analytical tools to investigate carbon nanotubes. This holds in particular as far as single wall carbon nanotubes (SWCNTs) are concerned. There are several reasons for this. Firstly, the structure of the tubes is rather simple and many properties can be derived to a first approximation from a study of zone folded planar graphene. Secondly, the Raman spectra of carbon phases are very well known and easy to record. Thirdly, for the SWCNTs resonance conditions are easily met for lasers operating in the visible spectral range. As a matter of fact under good resonance conditions, the Raman response from the tubes has the highest cross section of all materials known so far. Finally, many of the physical properties of the SWCNTs scale with the diameter and depend on the helicity of the tubes, like some of the Raman lines. Therefore the latter are appropriate to get information on such properties.

In this series of lectures three major subjects will be discussed:

- Fundamentals of Raman scattering
- Raman scattering of single wall carbon nanotubes
- Raman scattering of double wall carbon nanotubes

## 1. Fundamentals of Raman Scattering

Raman scattering in solids is the inelastic scattering of light from interaction with quasi-particles with an optical type of dispersion. This means for these particles $\omega(q) \neq 0$ even for $q = 0$. This contrasts the Raman process to Brillouin scattering where interaction of the light is with quasi particles with acoustic dispersion such that $\omega(q) = 0$ for $q = 0$. A general description of Raman scattering can be found in Refs[1-5].

### 1.1. FORMAL AND MATHEMATICAL DESCRIPTION OF THE RAMAN PROCESS

The classical approach for the scattering from solids considers the modulation of the susceptibility $\chi_{jl}(\omega)$ by the phonons. It is expanded with respect to the normal coordinate $Q_k$ of phonon $k$. The first expansion coefficient is the Raman tensor. Thus we obtain for the polarizability (in As/m$^2$) induced by the phonon $k$

$$P^D{}_j = \chi_{jl,k}(\omega,\Omega_k,t)\varepsilon_0 E_l(\omega,t) = \frac{1}{2}\varepsilon_0 \chi_{jl,k}(\omega,\Omega_k) Q_k E_{l0} Cos(\omega \pm \Omega_k)t \quad (1)$$

with

$$\chi_{jl,k} = \frac{\partial \chi_{jl}}{\partial Q_k}$$

Assuming that the induced polarizations act as the source of the evanescent radiation in the form of a Hertzian dipole we obtain for the emitted Raman light and a 90° scattering geometry as depicted in Fig.1, after thermal averaging,

$$\Phi_{yx,\overline{\Omega}} = \frac{\hbar(\omega \pm \Omega_k)^4 V_u \chi_{yx,k}{}^2 (n_k + 1) V}{32\pi^2 c_0{}^4 \Omega_k} I_i \qquad (2)$$

in [W/Ster], where $I_i$, $V_u$, V and $n_k = \exp(\hbar\Omega_k/K_B T^{-1})$ are the intensity of the incident light, the unit cell volume, the scattering volume, and the average Bose occupation number, respectively. From Eq. 2 we define the Raman cross section of the form

$$\sigma = \frac{1}{V I_i} \frac{d\Phi_{yx}}{d\overline{\Omega}} \ , \qquad (3)$$

where $d\overline{\Omega}$ is a differential solid angle.

In a quantum mechanical description the incident photon excites an electron-hole pair from a ground state $|0\rangle$ to an intermediate state $|i\rangle$. This transition does not need energy conservation. In the intermediate state a phonon is generated (or absorbed), either from the excited electron or from the excited hole, by electron-phonon interaction. This takes the system to another intermediate state $|f'\rangle$ from where the electron hole pair can recombine to the final state $|f\rangle$. This state is higher (lower) in energy as compared to the original ground state $|0\rangle$ by one phonon. Overall energy has to be conserved. In solids

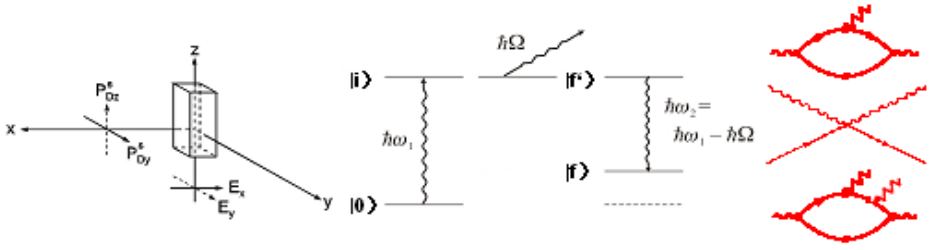


Fig. 1 Geometry for a $90^0$ Raman scattering experiment. Incident and scattered light are either parallel or perpendicular polarized to the scattering plane (left); Quantum-mechanical states involved in the scattering process (centre); Feynman graphs for the $H_{pA}$ interaction (phonon scattering, top), the $H_{AA}$ interaction (electron scattering, centre), and for a two phonon process (bottom)(right).

wave vector conservation is also required. This means: $\vec{k}_i = \vec{k}_s \pm \vec{q}$ where $k_i$ and $k_s$ are the wave vectors of the incident and scattered light, respectively, and $\vec{q}$ is the wave vector of the phonon. Accordingly, due to the small value of the wave vectors of visible light, in first order only phonons with $q \sim 0$ ($\Gamma$-point phonons) can contribute to the scattering process.

For a quantitative description of the quantum-mechanical formulation we can use the Feynman diagrams of Fig. 1 (right). For the one phonon Stokes process this yields

$$K_{2f,10} = \sum_{i,f} \frac{\langle \omega_2, f | H_{er} | 0, f \rangle \langle 0, f' | H_{ep} | 0, i \rangle \langle 0, i | H_{er} | \omega_1, 0 \rangle}{(E_1 - E_i - i\gamma\hbar)(E_2 - E_f - i\gamma\hbar)} \tag{4}$$

Where $H_{er}$ and $H_{ep}$ are the electron-radiation and the electron-phonon interaction Hamiltonians, respectively, $E_1$ and $E_2$ are the energy of the incident and scattered light, $E_i$ and $E_f$ represent all transition energies from the ground state and to the final state involved, and $\gamma$ is an inverse life time constant. The absolute square of this expression is proportional to the Raman cross section. The four indices of the symbol on the left hand side of the equation represent the two states |0> and |f> and the two phonons $\omega_1$ and $\omega_2$ involved.

If one or several transitions from Eq. 5 are to a real eigenstate, the cross section will be strongly enhanced and is easier to calculate as it will be dominated by these transitions. This case is particularly important for solids where the transition energies often exhibit a continuum in the visible spectral range, known as the *joint density of states* $g_{jds}(\varepsilon)$ . In this case we can replace the sum in Eq. 4 by an integral and obtain for the Raman cross section

$$\sigma(\omega_1) \propto \left| \int \frac{M_f M_{ph} M_0 \, g_{jds}(\varepsilon) \, d\varepsilon}{(\hbar\omega_1 - \varepsilon - i\hbar\gamma)(\hbar\omega_2 - \varepsilon - i\hbar\gamma)} \right|^2 \approx |M|^2 \left| \int \frac{g_{jds}(\varepsilon) \, d\varepsilon}{(\hbar\omega_1 - \varepsilon - i\hbar\alpha)(\hbar\omega_2 - \varepsilon - i\hbar\alpha)} \right| \tag{5}$$

where $M$ stands for the product of the three matrix elements on the left side.

## 1.2. RAMAN SCATTERING, EXPERIMENTAL

On the experimental side four basic components are needed for Raman scattering: a very narrow band light source, a light focusing and light collection optics, a monochromator system with very good stray light suppression and a very sensitive photon detector. A schematic of a Raman experiment is depicted in Fig. 2.

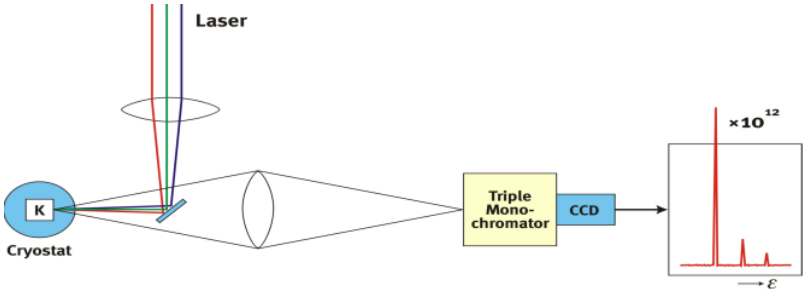


Fig. 2 Experimental set up for a Raman experiment, consisting of several lasers for excitation, a light focusing and light collection optic, the sample, the monochromator and an appropriate detector

As a light source almost exclusively lasers are used in the visible or near visible spectral range. A few mW of power are enough. Tunable lasers such as dye-lasers or Ti-Sapphire lasers are of high advantage if resonance scattering is the goal. The focusing and light collection system is either a conventional bright optics or a microscope. In special cases near field optics can be used. In this case spatial resolution goes down to about 40 nm. For the spectral analysis usually triple monochromators are used which can be operated in an additive or in a subtractive mode. In the former spectral resolution is higher and allows for a spectral band pass down to 0.5 $cm^{-1}$ for red lasers. In the subtractive mode stray light suppression is much better which allows measuring Raman shifts down to the one wave number region. Recently also single monochromators are in use (confocal Raman systems) in combination with very sharp cutting notch filers. The advantage of such systems is their very high brightness but each laser needs its own notch filter. For the detection of the Raman light almost exclusively nitrogen cooled, back-thinned, and, if necessary, blue enhanced CCD detectors are used.

Raman scattering has been widely applied to study crystalline and non-crystalline materials with respect to their structures, bonding, symmetries, morphologies, phase transitions etc. From the many applications two are selected here as they will be important for the following. Figure 3 depicts Raman spectra of various well known carbon phases. Diamond has cubic crystal symmetry and two atoms per unit cell. Therefore it has only one, but threefold degenerated optical mode. Graphite, at least as far as the graphene plane is concerned has also two atoms per unit cell but the symmetry is only hexagonal. Therefore it has two optical modes, one non degenerated $A_g$ species and one twofold degenerated $E_{2g}$ species. The latter is located close to 1600 $cm^{-1}$ and usually called G-line. The other two lines we see in Fig. 3 for the graphitic material are the D-line and the overtone of the D-line. The D-line is defect induced and only observed if at least some disorder is present in the material.

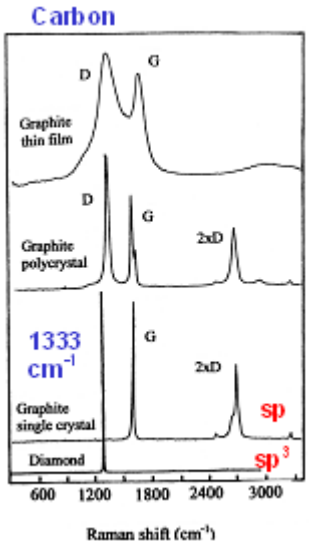


Fig. 3 Raman spectra for various carbon phases. Bottom: $sp^3$ bonded diamond, second, third, and fourth from bottom: $sp^2$ bonded carbons with increasing disorder.

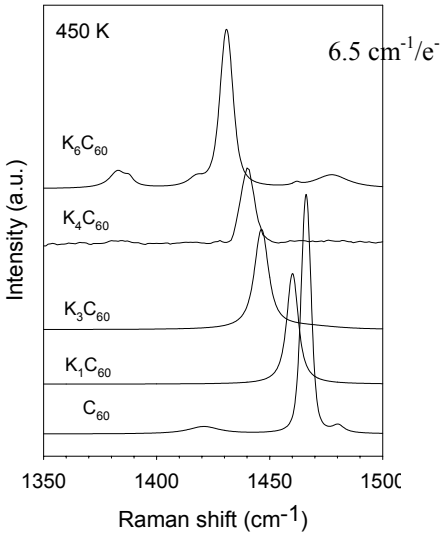


Fig. 4 Raman line of the pentagonal pinch mode in $C_{60}$ fullerene for various states of doping.

Interestingly, the overtone of this line is not defect induced. Neither lines originate from Γ-point phonons and are very famous in $sp^2$ carbon systems. Figure 4 depicts Raman spectra of the pentagonal pinch mode of $C_{60}$. In pristine material the line is strongly resonance enhanced, particularly in the green-blue spectral range, and located at 1468 $cm^{-1}$. If electron donors such as e.g. alkali metals are intercalated electrons are transferred from the metal to the fullerene orbitals and the conduction band fills up. This causes a quasi-linear downshift of the pentagonal pinch mode by about 6.5 $cm^{-1}$ per transferred electron. This downshift has been used widely to determine the charge state of $C_{60}$ in charge transfer $C_{60}$ compounds.

## 1.3. SPECIAL TECHNIQUES IN RAMAN SCATTERING

### RESONANCE EXCITATION

Since Raman scattering involves not only electron-phonon interaction but also light induced electronic transitions, information on the latter can be obtained. This is in particular so for resonance scattering. A resonance profile of a Raman line represents the cross section as a function of excitation energy. The peak in the profile locates the resonance transition. Since all components of the Raman equipment are sensitive to the light energy, careful calibration is needed. This is

usually done by measuring the spectrometer response of a well known cross section such as e. g. the one of the 520 $cm^{-1}$ Raman line in Si. In this way electronic transition energies can be determined even from powdered material or from thick, non transparent films.

## FANO-BREIT-WIGNER LINE SHAPE

Another interesting possibility is the observation of Raman scattering from free electrons in metals or degenerate semiconductors. In this case the $H_{AA}$-term of the perturbation Hamiltonian becomes relevant and the excited Raman states exhibit a continuum. Unfortunately, the $H_{AA}$ perturbation is very small and the electronic Raman effect is therefore difficult to observe. However, if the electronic continuum couples to a phonon, interference effects deform the line shape of the latter and the response of the electron continuum becomes observable. The situation is depicted in Fig. 5. It shows the response from a Si crystal doped to various hole-concentrations and excited with a red laser. For weak interaction (low doping) the Raman line becomes asymmetric and broadened. For stronger interaction the line shape almost inverts.

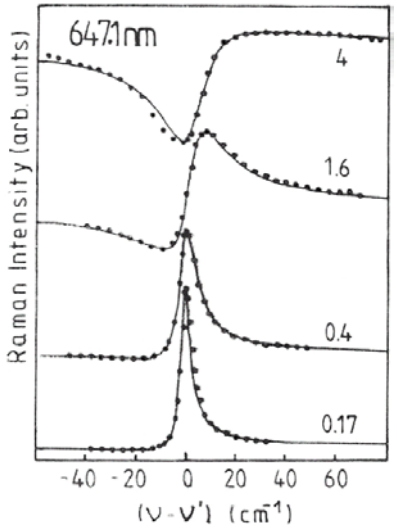


Fig. 5 Fano-Breit-Wigner line shapes for the $F_{2g}$ mode in Si doped to various concentrations as indicated in units of $10^{20}$ $cm^{-3}$, after [6].

## DISPERSIVE MODES

According to the Raman concept the distance of the Raman line from the exciting laser should be independent of the laser energy. This is not always the case. If the Raman shift depends on the energy of the exciting laser we talk

about *dispersive Raman lines*. There can be several reasons for a dispersion of the Raman lines as for example

- Photo-selective resonance scattering in optically inhomogeneous material
- Carrier depletion at surfaces combined with light penetration effects
- Scattering from non $\Gamma$-point phonons where the dispersion of the phonon mode becomes relevant and double resonance scattering applies.

In optically inhomogeneous material the laser depicts predominately such parts where its energy matches to the optical gap. Since vibrational frequencies often also scale with the optical inhomogeneity, dispersion is observed for such lines.

Depletion of carriers happens at surfaces of semiconductors by surface state effects. This means any contribution of the carriers to the phonon force constants is modulated with distance from the surface. Since the penetration of light depends on its energy, light of different energies will probe different regions of the crystal with respect to distance from the surface and line dispersion will be observed. An example is shown in Fig.6 for p-doped Ge.

Line dispersion for scattering from non $\Gamma$-point phonons is very famous for the D-line in graphite and plays an important role for SWCNTs. Figure 7 depicts an experimental result for the shift of the D-line with laser excitation. The shift is approximately 43 $cm^{-1}$/eV, independent from the amount of disorder. The D-line represents a *K*-point phonon which becomes Raman allowed by a double resonance scattering. The individual intermediate steps of the scattering processes are depicted in the insert of the figure. First, an electron–hole pair is excited under resonance conditions. Then a K-point phonon is generated and scatters the electron from *K* to *K'*, again in resonance, since it ends up at an eigenstate of the graphene bands. In order to satisfy q-conservation an electron is now elastically and non resonant back scattered to the *K*-point region by an impurity. From there it recombines non-resonantly with the hole. This double resonance scattering process is well known from semiconductor Raman scattering[7]. In the case of overtone Raman scattering which leads to the G'-line in graphite, backscattering of the electron is established by another phonon. Therefore no impurity scattering is required.

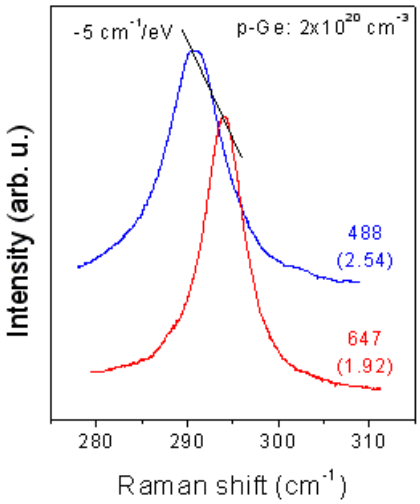


Fig. 6 Raman line of p-doped Ge as excited by two different laser lines, after [8]

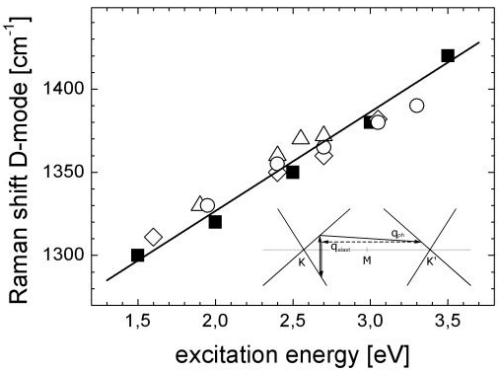


Fig. 7 Shift of the D-line in polycrystalline graphite versus laser excitation energy, after [9]. The insert depicts the graphite band structure close to the K- and K'- points of the Brillouin zone and the scattering process for the double resonance

## 1.4. THE ELECTRONIC STATES OF SINGLE WALL CARBON NANOTUBES

### RESULTS FROM ZONE FOLDING

Zone folding in the graphene plane is the simplest way to obtain the band structure of SWCNTs. This process will not be described here in detail, since other reports deal with it sufficient explicitly. General descriptions of the electronic properties of SWCNTs can be found in Refs[10-12]. Only properties with immediate connection to the Raman or resonance Raman process will be described.

By the zone folding process a discrete set of curves is cut out from the band structure of graphene which represent the band structure of the SWCNTs. Maxima and minima in these $\varepsilon(k)$ relations lead to the set of van Hove singularities in the density of electronic states which determine, at least in a first approximation, the optical and resonance Raman behavior of the tubes. Figure 8 depicts the density of states for two selected tubes in a narrow energy range around the Fermi level. The (10,10) tube is clearly metallic and the (11,9) tube is semi-conducting. In this approximation only transitions between symmetric Van Hove singularities are allowed and usually assigned as $E_{ii}^{S}$ or $E_{ii}^{M}$ for the

semi-conducting and metallic tubes, respectively. The energies $E_{ii}^{S}$ and $E_{ii}^{M}$ scale with the inverse tube diameter approximately as

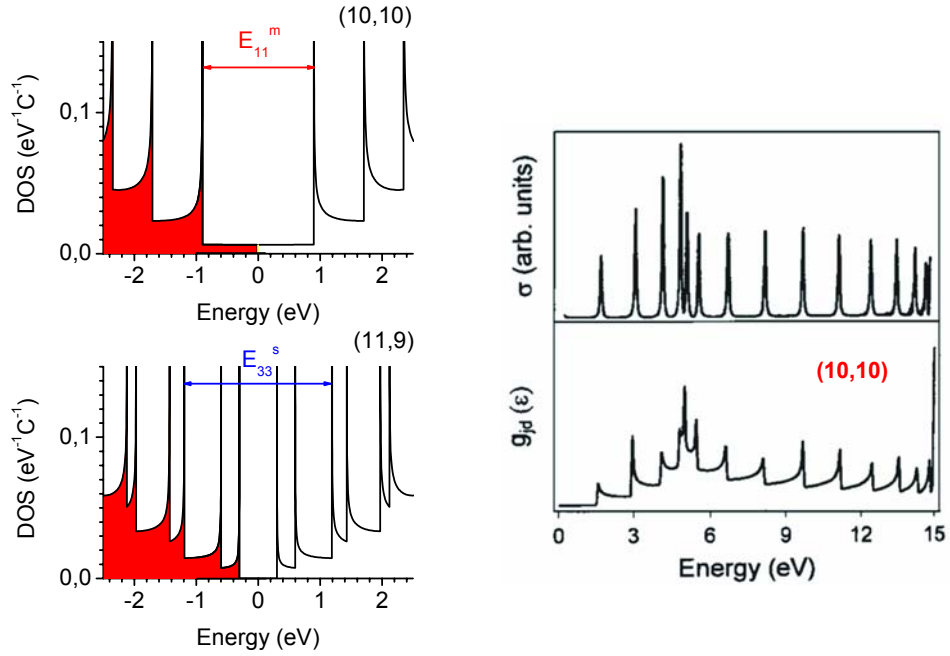


Fig. 8 Van Hove singularities for a (10,10) and for a (11,9) tube (left panel) and calculated joint density of states and Raman cross section for a (10,10) armchair tube (right panel).

$$E_{ii}^{S} = \frac{2V_0 a_{cc} i}{D} = \frac{0.85i}{D}, \qquad E_{ii}^{M} = \frac{6V_0 a_{cc} i}{D} = \frac{2.55i}{D} \tag{6}$$

where $V_0 = 2.9$ eV is the ππ- overlap and $a_{cc} = 0.144$ nm is the carbon-carbon distance in graphene. There is a hierarchy if corrections to these values for the real tube states. These corrections include: trigonal warping in the graphene band structure, chirality effects, curvature effects, and electron correlation (excitonic behavior). For a quantitative analysis of the tubes these corrections are important as it will be discussed later.

For the achiral tubes the joint density of states can be evaluated analytically in the zone folding approximation. For armchair tubes (n,n) it yields

$$g_{jds}^{AC}(\varepsilon, n) = \sum_{q} \frac{\varepsilon}{\pi a \gamma_0^{\,2} \sin\left[k_q(\varepsilon)a/2(\cos(q\pi/n) - 2\cos(k_q(\varepsilon)a/2)\right]} \tag{7}$$

where the sum runs over all sub-bands. This relation allows calculating the Raman scattering cross section explicitly using Eq. 6. The result of the integration is depicted in Fig. 8, right panel.

**THE KATAURA PLOT**

The linear relation between transition energies and inverse tube diameter allows plotting the whole set of transition energies on a map called Kataura plot[13] as shown in Fig. 9. The straight lines represent the relations of Eq. 5. The deviation of the points from the lines originates from trigonal warping and from chirality effects.

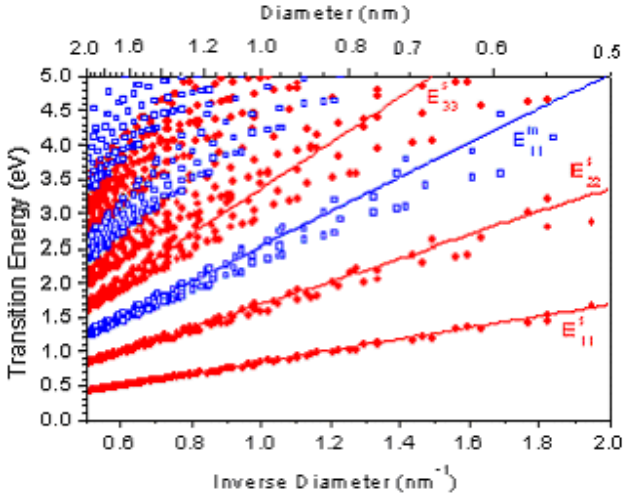


Fig. 9 Linear relation between transition energies and inverse tube diameter. Each symbol represents one transition in one particular tube. Full circles are semi-conducting tubes, open squares represent metallic tubes.

## 2. Raman Scattering of Single Wall Carbon Nanotubes

Due to its strong resonance character the Raman spectrum of SWCNTs is easily recorded and has very pronounced lines. The latter discriminates the SWCNT spectra from those of mulitwall carbon nanotubes where usually only a broad G-line and a rather broad D-line, together with its overtone, is observed. For the SWCNTs each Raman line behaves special as it will be discussed below. The discussion will also be extended to filled tubes, especially for filling with fullerenes.

## 2.1. BASIC RAMAN LINES OF SINGLE WALL CARBON NANOTUBES

The Raman spectrum of SWCNTs has four characteristic lines: the radial breathing mode (RBM), the defect induced line (D-line), the graphitic line (G-line), and the overtone of the D-line (G'-line). The D-, G-, and G'-line are equivalent to lines in graphite but the RBM does not exist there (or has zero

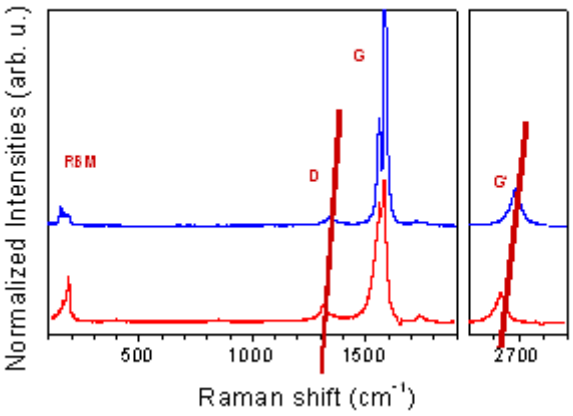


Fig. 10 Raman spectra of SWCNTs with a mean diameter of 1.36 nm as excited with 488 nm laser (upper spectrum) and 647 nm (lower spectrum).

frequency). Figure 10 depicts two Raman spectra of laser ablation grown SWCNTs as excited with two different lasers. The four characteristic modes are assigned. The inclined lines passing through the peaks of the D- and G'-lines indicate the dispersive behavior of these modes.

The position of the RBM scales as 1/D where D is the tube diameter. This, together with the above described scaling of the transition energies, leads to a dispersive behaviour which manifests itself in a dependence of the line shape on the laser energy. The G-line has also some structure which will be discussed in detail below. Like in graphite, the intensity of the D-line increases with defect concentration whereas the G'-line is independent of defects.

Group theory is an important approach to Raman analyses. In principle line groups are needed to describe the symmetry properties of the tubes. Symmetry elements, point groups and number and species of Raman active modes are summarized in Tab. 1. Each nanotube has a rotation axis and a screw axis parallel to the tube axis, in addition to the trivial translations. The counting of the rotation axis is determined by the number of lattice points n(LP) on the chiral vector. This number is given by the greatest common divisor between m

and n. In addition to the rotational axes along the tube axis each tube has two types of twofold rotation axes perpendicular to the tube axis. Achiral tubes have some additional symmetry elements. Since we are mainly interested in q = 0 phonons, we can study the isogonal point groups related to the line groups which are $D_n$ and $D_{nh}$ for the chiral and for the achiral tubes, respectively, with $n = N(R) = N_R$ . $N_R$ is the number of rings in the unit cell. In this way we find 8 and 14 Raman active modes for the achiral and chiral tubes, respectively. Raman tensors are tabulated in classical textbooks like e. g. [3]. The RBM is total symmetric and has $A_{1g}$ ($A_1$) symmetry. The G-line has $A_{1g}$, $E_{1g}$, and $E_{2g}$ ($A_1$, $E_1$, and $E_2$) components.

| Symmetry elements: | Point groups |
|---|---|
| Line groups with SE<br>T: translations,<br>$C_{n(LP)}^{s}$: rotations, $2\pi/n(LP)$, parallel<br>$C_{n(LP)}^{w}$: screw axes, $\pi/n(LP)+a/2$, parallel<br>U, U‘: rotations, $\pi$, perpendicular<br>$\sigma_h$, $\sigma_v$, $\sigma_h^{‘g}$, $\sigma_h^{‘rrfl}$: additional mirror planes, one mirror glide plane, and one roto-reflexion plan, only for achiral tubes | For q = 0 modes only the isogonal point groups to the line groups are relevant. Theses are $D_{N(R)}$ and $D_{N(R)h}$ for the chiral and achiral tubes, respectively, where N(R) is the number of rings in the unit cell<br><br>Irreducible representations for $D_n$ and $D_{nh}$:<br>only 1-dimemsional and 2-dimensional: A, B, E<br>achirals have centre of inversion -> g,u<br>e.g. chirals: $A_1$, $A_2$, $B_1$ $B_2$, $E_1$, $E_2$ ...$E_{N(R)/2-1}$ |
| Raman active modes:<br>$\Gamma_{ZZ}^{Raman} = 2A_{1g}+ 3E_{1g}+ 3E_{2g}$, zigzag<br>$\Gamma_{AC}^{Raman} = 2A_{1g}+ 2E_{1g}+ 4E_{2g}$, armchair<br>$\Gamma_{Cl}^{Raman} = 3A_1+ 5E_1+ 6E_2$, chiral | 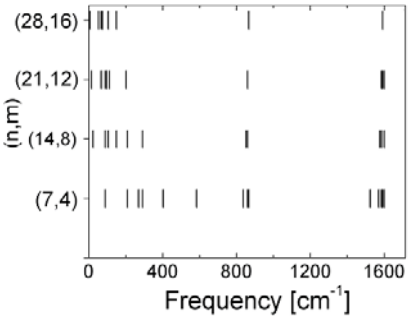 |

Table 1 Summary of group theoretical properties of SWCNTs; The lower right graph depicts calculated Raman lines for a set of metallic SWCNTs, after [14].

The calculated frequencies in the lower right part of the table were obtained from zone folding of the graphene plane (except for the RBM mode). As SWCNTs tend to assemble into bundles where tube-tube interaction has some influence on the frequencies such frequencies may not immediately correspond to measured Raman modes.

## 2.2. SPECIAL RAMAN MODES

Now we will discuss the four special Raman modes in some detail.

### THE RADIAL BREATHING MODE

The RBM suffers to some extent from the tube-tube interaction in the bundles. Therefore its experimentally observed frequency is formally described by

$$\nu_{RBM} = C_1 / D^x + C_2 \tag{10}$$

where $C_1$ and $C_2$ are constants and x is very close to 1. Unfortunately, both constants vary from report to report in a rather wide range which makes it difficult to determine the tube diameter from the observed frequencies, even if Raman experiments were carried out on individual tubes. On the other hand the Raman response from the RBM mode of a sample with distributed diameters exhibits an interesting oscillatory dispersion as depicted in Fig. 11, left panel. In the figure the RBM Raman line pattern are plotted for a large number of exciting lasers. The origin of the oscillations is explained in the right panel of the figure. The straight lines on the right represent the Kataura plot. The dashed line on the left represents Eq. 8, without the constant $C_2$. If a red laser excites a tube resonantly with transition $\varepsilon_3$, a RBM frequency will be observed as given

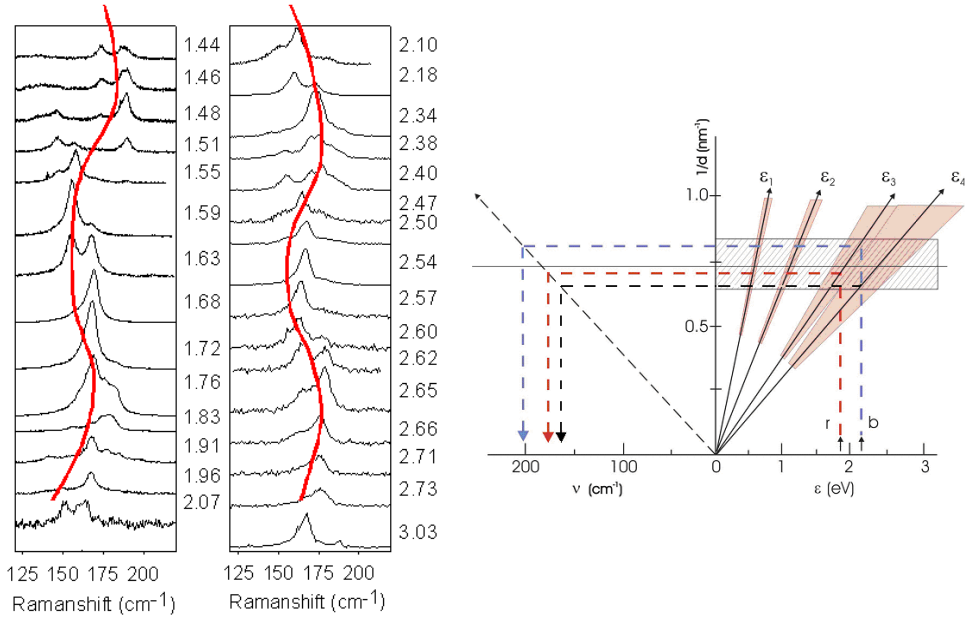


Fig. 11 Raman response of the RBM as excited for many different lasers, after [15]. The wavy line is a guide for the eye (left); The right panel depicts a schematic for the resonance excitations. $\varepsilon_i$ are the transition energies, r and b represent red and blue lasers. ν is the RBM frequency.

by the dashed line connection. Shifting the laser energy upwards, the observed RBM frequency will also move upwards as thinner tubes will get into resonance. However, at some point the laser will also be able to excite in resonance rather large tubes with the next higher electronic transition, which would be $\varepsilon_4$ in the assignment of the figure. Then, the first moment of the total RBM response will start to decrease. Thus, the observed oscillations in frequency can be traced back to the jamming of the electronic states into the van Hove singularities.

The well defined response of the RBM mode to the distribution of the tube diameters can be used to determine the diameter distribution function. In fact by analyzing the first and the second moment of the RBM response and assuming a Gaussian distribution for the tube diameters one can evaluate the mean and the variance of the Gaussian function[15]. An even better and more reliable way is to measure the RBM response with two or three different lasers and obtain in a redundant manner the parameters for the Gaussian function from this procedure.

Recently some more detailed Raman experiments were carried out for the HiPco material. These tubes have usually a mean tube diameter of only 1 nm but a rather large width for the distribution function. Results for the RBM response are depicted in Fig. 12, left panel, as exited for various lasers. The oscillatory behavior is certainly also observed but a lot of individual lines

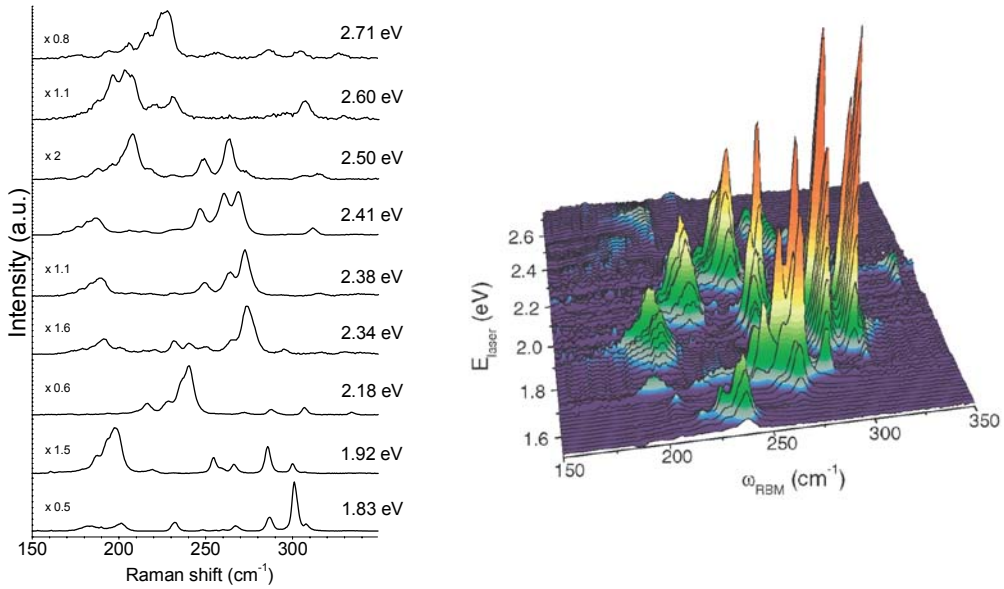


Fig. 12 Raman response for the RBM mode of HiPco tubes (left), after [16]; Raman cross sections as plotted over a 2D grid of RBM frequency and laser excitation energy, after [17].

appear, wide spread on the frequency axis. It is possible to measure for each of the peaks the resonance profile. The results can be plotted on a two-dimensional grid of frequency and laser excitation energy. As a result we obtain a so called "Raman chard". An example for a Raman chard is depicted in Fig. 12.

Another important result for the Raman response comes from spectra

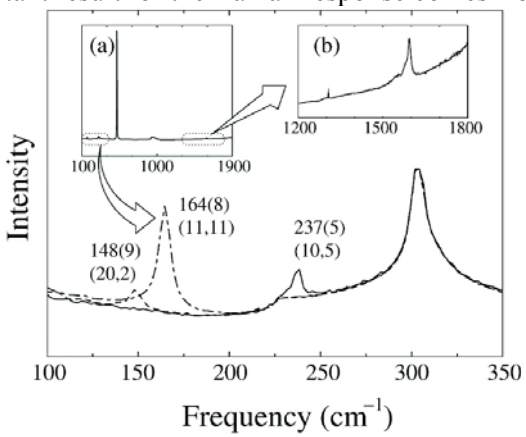


Fig. 13 Raman spectra of the RBM modes at 148, 164, and 237 cm-1, respectively. The line at 300 cm$^{-1}$ comes from Si; after [18]

recorded for individual tubes. Since the resonance cross section is so large spectra could be measured from a scattering volume as low as $10^{-6}$ μm$^3$. This is the volume of one SWCNT in a laser focus of 500 nm diameter. Figure 13 gives an example. The line from Si originates from an impurity activated mode and is about 50 times smaller than the Raman response of the Si optical mode. Estimating the scattering volume for Si to be 0.2 μm$^3$ we find the Raman cross section of SWCNTs more than a factor $10^6$ larger as compared to Si.

**THE G-LINE**

From a theoretical consideration the G-line in SWCNTs consists of six components with $A_1$, $E_1$, and $E_2$ symmetry and longitudinal or transversal (= circumferential) orientation of the normal coordinates. For the achiral tubes the index g must be added as usual. Experimentally indeed a more or less expressed fine structure has been reported for the G-line pattern. An exact assignment of the fine structure to the A and E modes was not possible so far. The G-line does not exhibit dispersion except when it comes to the excitation of the metallic tubes. However, the G-line exhibits an oscillatory behavior with respect to line intensity if the laser energy is tuned. This is demonstrated Fig. 14, left panel. The set of spectra represent the G-mode response as excited for various lasers. Starting with the highest laser energies line intensities increase down to about

2.49 eV. For a further reduction of the energy the main peak of the G-line decreases but a broad structure appears about 40 $cm^{-1}$ downshifted.

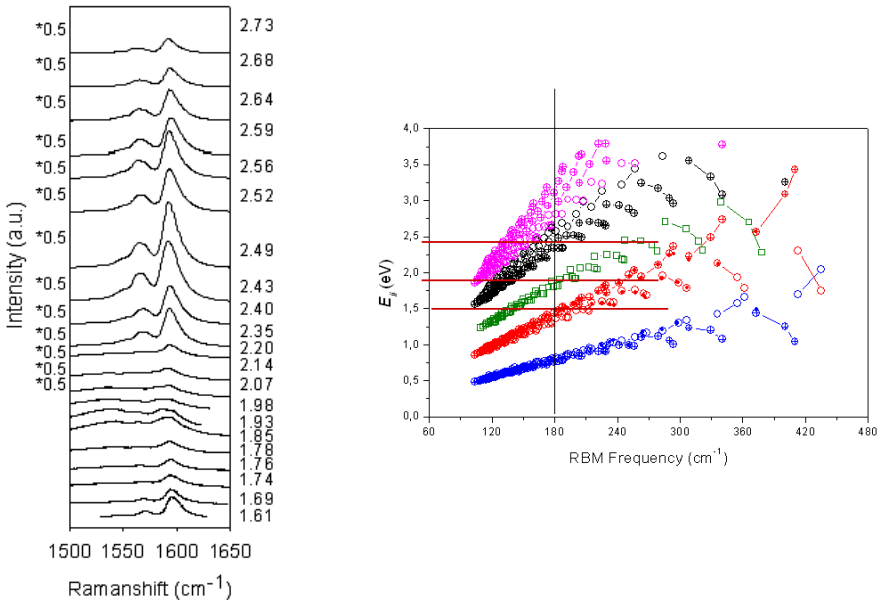


Fig. 14 Raman response for the g-line as excited for various lasers; Spectra are normalized in intensity; (left), after [19]; Kataura plot of transition energy versus RBM frequency, including curvature effects, after [20]; horizontal lines are energy markers.

This broad feature peaks for about 1.93 eV excitation and decreases again for further reduction of the excitation energy. Simultaneously the main peak of the G-line starts to grow again. The right part of the figure depicts a modified Kataura plot. The calculation was performed on the level of symmetry adapted non orthogonal tight binding wave functions which allow to consider curvature effects. The deviations from the linear behaviour are particularly strong for the small diameter tubes (high frequency RBMs). For the tubes used in Fig. 14, left side, then mean diameter was 1.4 nm which corresponds to an approximate RBM frequency of 180 $cm^{-1}$. The three horizontal lines mark the energies where the main G-line peaks for the first time, where the broad sideband peaks, and where the main G-line peak approaches a peak again. Considering the diameter of the tubes (or the mean RBM frequency of 180 $cm^{-1}$) it is obvious, that the first peak of the G-line coincides with the resonance at the $E_{33}^{S}$ transition. The maximum of the broad sideband occurs for resonance excitation of the metallic tubes at the $E_{11}^{M}$ transition and the re-increase of the main peak takes place when the laser energy comes down to the $E_{22}^{S}$ transition for the semi-conducting tubes. A blow up of the response from the metallic tubes

exhibits a Fano-Breit-Wigner line shape demonstrating the strong coupling of this particular line with the free carriers in the metallic tubes.

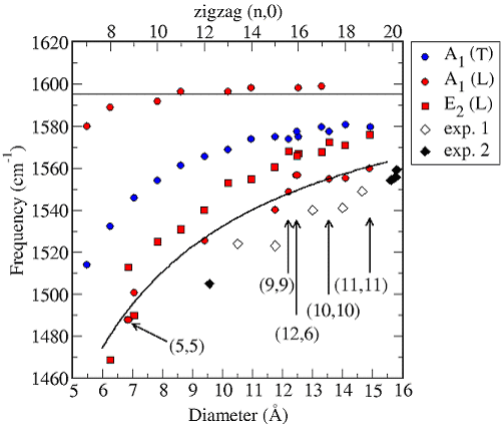


Fig. 15 Frequencies for the G-line as calculated from the Vienna Ab initio Simulation Package (VASP), after [21]; The full drawn line is an empirical approximation.

The frequencies of the G-line components were calculated ab initio by DFT for armchair and zigzag tubes. Results are depicted in Fig. 15 for the three selected components $A_1(T)$, $A_1(L)$, and $E_2(L)$. Experimental results for the line position of the metallic tubes are also included in the figure. Two results are striking. The dependence of line frequency on tube diameter is small for the A modes as long as the tube diameters are rather large. Only for very small tubes a considerable deviation from the limiting value for large tubes is observed. Only the $E_2(L)$ mode exhibits a considerable down shift with decreasing tube diameter. The other important result is the dramatic drop of line frequencies for the metallic species of the $A_1(L)$ modes. This mode softening corresponds exactly to the experimentally observed downshift of the Raman response for the metallic tubes. A special Peierls-type electron-phonon coupling mechanism was found to be responsible for this softening. This mechanism operates only for the $A_1(L)$ frequencies. The full drawn line represents an empirical law of the form $\nu = 1619 - 866/D$ [22].

There were several reports concerning the change of the G-line Raman response on doping with electron donors and electron acceptors. The general observation is a quenching of the resonance enhancement as a consequence of filling the conduction band (or depleting the valence band). Figure 16 depicts an example where arc discharge grown SWCNTs were intercalated with Li. The dramatic decrease of the lower frequency components and a weak up shift of the high frequency component is observed. Obviously the metallic tubes run out of resonance more rapidly.

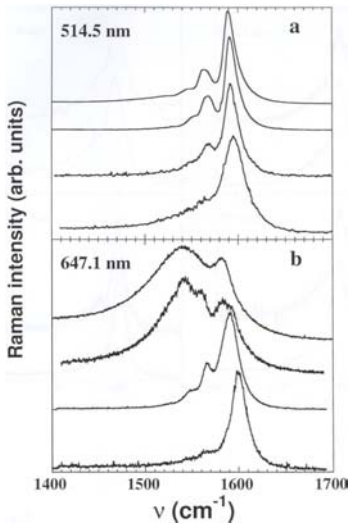


Fig. 16 Raman response of the G-line as excited with two different lasers after doping with Li. The Li concentration increases from top to bottom; after [23]

**THE D-LINE AND THE G'-LINE**

The D-line and the G'-line exhibit a quasi-linear linear dispersion. A set of

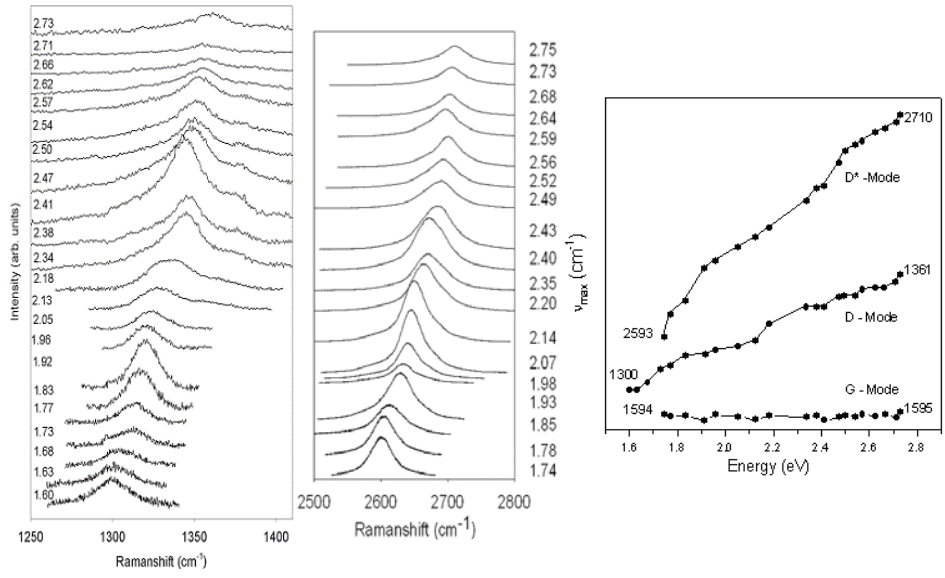


Fig. 17 Raman spectra for the D-line (left) and for the G'-line (center) as excited for various lasers. The right part of the figure depicts peak positions of the lines versus laser energy. D* is equivalent to G' The G-line is included for comparison; after [24]

spectra for both lines is depicted in Fig. 17. The intensity profiles represent again the resonance transitions from the Kataura plot. The right part of the figure shows the shift of the lines with increasing laser energy explicitly. For comparison the completely flat dispersion for the G-mode is also depicted. The slope of the quasi-linear behavior is 42.3 $cm^{-1}$/eV for the D-line and 86.4 $cm^{-1}$/eV for the G'-line. Both values are very similar to the values for graphite. Therefore it is obvious that the dispersion for the SWCNTs originates from K-point phonons like in graphite. However, since there is a difference in the electronic structure between the two systems, one would expect also some difference in the dispersion. This is indeed the case as we can observe an oscillatory behavior on top of the linear relation. A quantitative analysis revealed indeed that the oscillations originate from the jamming of the electronic states into the van Hove singularities[24]. This means the oscillatory behavior is a consequence of the triple resonance effect relevant for the SWCNTs.

## 2.3. FILLING CARBON NANOTUBES (PEAPODS)

One of the many interesting features observed for SWCNTs is the possibility to fill the tubes with other materials. Many different fillers were successfully incorporated into the tubes so far. One of the most exciting filling material are fullerenes. There is obviously a very strong cohesive force which attracts the fullerenes to the interior of the tubes. The classical and historically first observation of fullerenes inside the tubes came from transmission electron microscopy (TEM)[25]. However, since the tubes are at least partly transparent to visible light a Raman response from the fullerenes inside the tubes can also be expected. This has been demonstrated in various reports even though some of the fullerene modes appear as very weak lines. The line position of the pentagonal pinch mode is downshifted by 3 wave numbers as compared to the response from the free $C_{60}$ molecule and exhibits a characteristic line splitting[26].

Like the empty tubes the peapods can be doped with electron donors such as Rb. For a reasonably strong doping not only the Raman response from the tubes is modulated as expected from Fig. 16 but also the response from the pentagonal pinch mode is downshifted. For heavy doping the mode shifts by 37 $cm^{-1}$ which corresponds roughly to a charge transfer of 6 electrons. Thus, $C_{60}$ has adopted a charge state –6. This is demonstrated in Fig. 18, left frame for excitation with three different lasers. The simultaneously doped pristine tubes do not exhibit the fullerene line. The center of the figure depicts the radial part of the spectrum

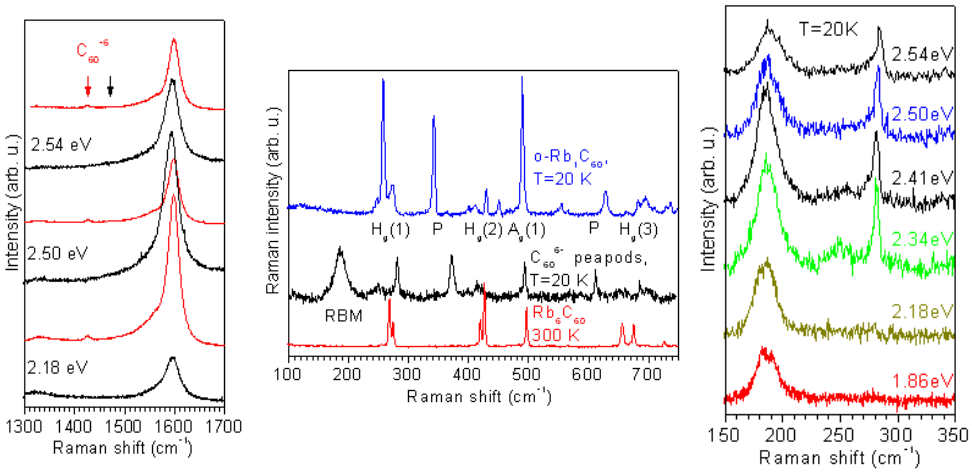


Fig. 18 Raman spectra of doped peapods in comparison to un-doped peapods and doped pristine tubes; G-line for doped peapods as compared to doped pristine tubes for three different laser excitations (left); RBM spectral region for doped peapods as compared to polymeric fullerenes and $Rb_6C_{60}$ (center); blow up of RBM spectral region for doped peapods (right); after [27]

and compares the response from the doped peapods with the Raman spectrum of $Rb_6C_{60}$ and the orthorhombic polymeric phase $RbC_{60}$. In the peapod spectrum two additional lines appear which are assigned as P and clearly indicate that the $C_{60}^{-6}$ molecules inside the tubes are polymerized. Calculations on the tight binding level suggested that this polymer is single bonded[28]. Interestingly, due to the doping the resonance behavior for the RBM of the tubes is lost and with it also the dispersion. This is demonstrated in the right panel of Fig. 18.

## 3. Raman scattering of double wall carbon nanotubes

Double wall carbon nanotubes (DWCNTs) are an other new species in the family of carbon nanophases. They are of particular interest if grown from peapods, since then there is exactly one inner tube in one outer tube. DWCNTs exhibit several remarkable features. They have the same small size as the SWCNTs but are stiffer and therefore more appropriate as mechanical sensors. Field emission is enhanced. The inner tubes have a very high curvature and allow therefore to study curvature effects in great detail. Inner shell tubes are grown in a highly shielded environment without catalyst and are therefore highly unperturbed. The outer tubes may be subjected to functionalization while the inner tubes remain untouched. Alternatively, as it will be shown below, the inner tubes may be modified e. g. by isotope substitution whereas the outer tubes remain as grown.

## 3.1. THE RAMAN RESPONSE FROM THE INNER TUBES

The growth of inner tubes from peapods by annealing at thigh temperatures was first demonstrated by Smith et al.[29] and proven by TEM. Like in the case of the peapods Raman spectroscopy is an other possibility to study the transition process. Figure 19 depicts a series of spectra which

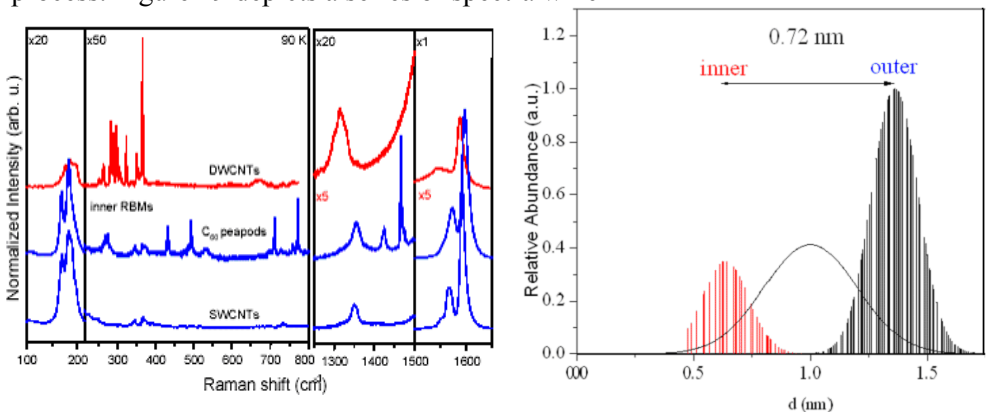


Fig. 19 Left: Raman spectra for SWCNTs, as exited with 514 nm (bottom), for peapods as exited with 488 nm (center) and for DWCNTs as excited with 647 nm (top). Right: Diameter distribution plotted as two histograms for outer shell and inner shell tubes and as a curve for HiPco material.

demonstrate the transition from peapods to DWCNTs. Annealing was performed for two hours in high vacuum at 1500 K. The difference in the spectra recorded for the peapods and for the DWCNTs clearly demonstrate the transition. In the spectrum of the DWCNTs all the lines from the fullerenes have disappeared and a new set of very sharp lines appeared around 300 cm$^{-1}$. As the inner tubes have a much smaller diameter this set of lines is obviously the response from the RBM of the latter. Note that for the red laser the response from the inner tubes is much larger than the response from the outer tubes, even though there is much less carbon material in the former. The right part of the figure depicts a histogram of the diameter distribution. It was drawn under the assumption that the wall to wall distance between inner and outer tube is 0.36 nm which means very close to the plane to plane distance in graphite. From this figure three important results can be depicted: Firstly, the number of carbon atoms in the inner tubes is only about one third of the carbon atoms in the outer tubes. Secondly, the distribution of the geometrically allowed tubes is much coarser for the inner tubes as compared to the outer tubes. And finally, there is a cutoff for the inner tube diameters just below d = 0.5 nm. The mean diameter of the inner tubes is about 0.7 nm.

The sharp lines recorded for the Raman response from the inner tubes are surprising. Measuring the response from the these tubes at low temperature and in the high resolution mode of the spectrometer revealed line widths down to

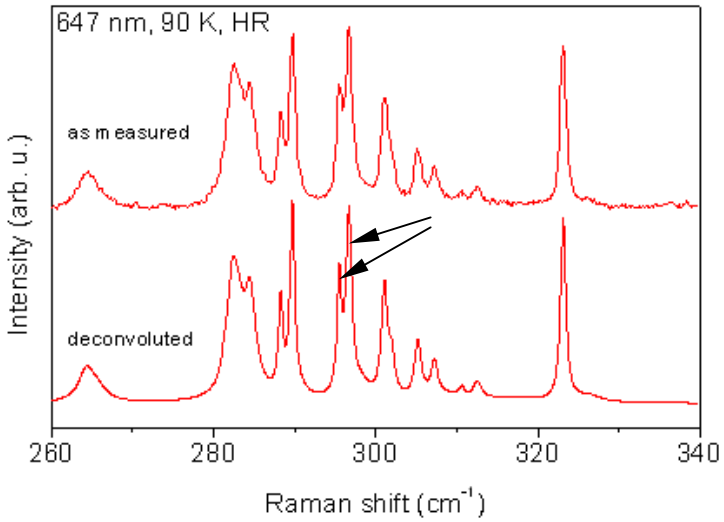


Fig. 20 Raman response of the RBM from the inner tubes as recorded with a resolution of 0.5 $cm^{-1}$ (top) and after deconvolution from the spectrometer response (bottom). The arrows indicate line splitting

0.4 $cm^{-1}$ after deconvolution from the spectrometer response. An example is depicted in Fig. 22. The narrow lines indicate a long phonon life time and therefore a highly unperturbed tube material. In addition to the small line width the figure also demonstrates a characteristic line splitting. As a result of this splitting the number of observed lines is considerably larger than the number of geometrically allowed tubes which can be accommodated in the interior of the host tubes. To a first approximation this can be explained by the lower density of geometrically allowed tubes with smaller diameter. Several outer tubes with increasing diameter may be considered as a host before the next larger inner tube can grow for best matching conditions. Since the tube-tube interaction shifts the RBM frequency, and since this interaction depends on the wall to wall distance between the tubes some splitting of the lines can be expected. (See also the discussion below.)

### 3.2. MODE ASSIGNMENT AND HIGH CURVATURE EFFECTS

Recording the Raman response with a large number of laser lines revealed the Raman response from all inner tubes in the diameter range from 1.1 nm down to 0.5 nm. Since the distribution of the RBM frequencies is not a smooth function with the diameters, a best fit search for the assignment of the modes to the (n,m) values of the corresponding tubes was possible. The result was reported in [30] and revealed a well defined straight line for the relation between RBM

frequency and inverse tube diameter of the form $\nu_{RBM} = C_1/D + C_2$ with $C_1 = 234$ cm$^{-1}$nm and $C_2 = 14$ cm$^{-1}$.

A more dramatic demonstration of the high curvature effects can be obtained from an analysis of the high frequency modes such as the G' mode. The Raman response for this mode as excited with various lasers is depicted in Fig. 21. The dispersion effect is clearly visible for the outer shell tubes (higher frequency

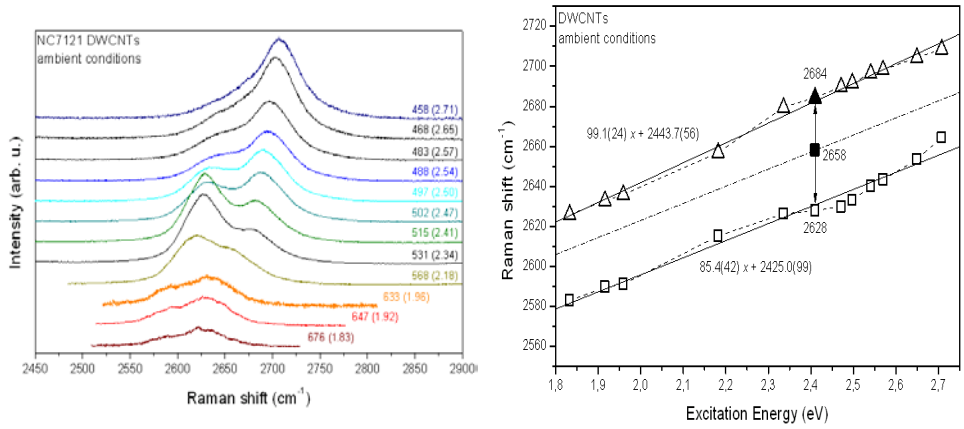


Fig. 21 Left pannel: Raman response of the G' mode of DWCNTs for various lasers as indicated. The high and the low frequency peaks come from the outer and inner shell tubes, respectively. The right pannel of the figure depicts the dispersion of the two modes. The value of 2658 cm$^{-1}$ for excitation with a green laser (2.42 eV) was obtained for an extrapolation from low curvature tubes.

peak) and for the inner shell tubes (lower frequency peak). A quantitative display of the dispersion is depicted in the right panel of the figure. The slopes for the inner and outer tubes are 85.4 and 99.1 cm$^{-1}$/eV, respectively. From an analysis of tubes with different diameters in the range of 1 to 1.4 nm an empirical relation of the form

$$\nu_{G'} = 2536 - 21/D \qquad (5)$$

was obtained in [31] for the dependence of the G' frequency on the tube diameter. This relation yields the correct value of 2684 cm$^{-1}$ for the outer tube if the spectrum is excited with a green laser but a much too high value of 2658 cm$^{-1}$ for the inner tubes. The observed value is 2628 cm$^{-1}$ which means 30 cm$^{-1}$ lower as expected from the extrapolation of Eq. 5. This difference is considered as a breakdown of Eq. 5 for high curvature tubes.

### 3.3. ISOTOPE SUBSTITUTION

It was demonstrated recently that the inner tube can be grown as in a highly $^{13}C$ enriched form by using $^{13}C$ enriched fullerenes as a filling material[32]. From the mass enhancement all vibrational modes are expected to shift downwards according to the concentration of $^{13}C$ used. This is demonstrated in

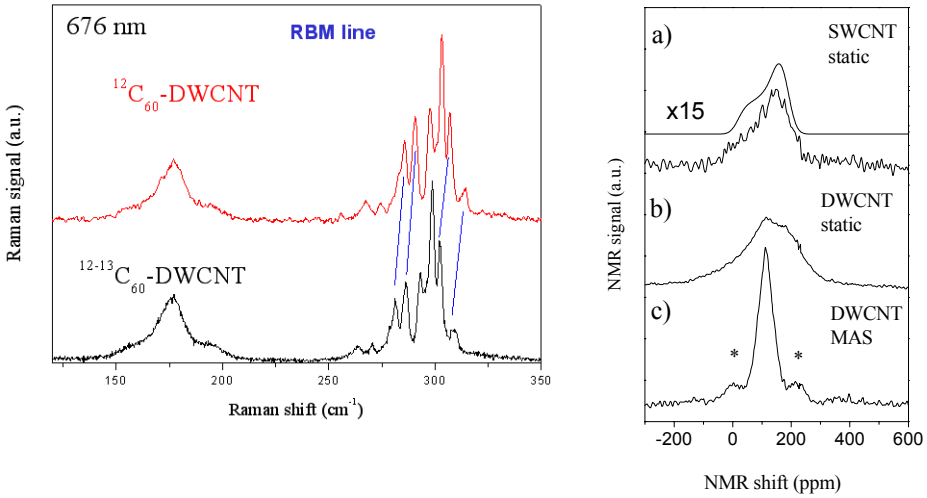


Fig. 22 $^{13}C$ substitution in carbon nanotubes; Left: Raman response for the RBM line; Right: NMR spectroscopy of carbon nanotubes. Top: Response of static NMR for non enriched SWCNTs. The full drawn line is a calculated fit. Center and bottom: static NMR and MAS NMR, respectively, for highly $^{13}C$ enriched inner shell tubes.

Fig. 22, left panel, for the RBM. The downshift demonstrates the mass enhancement.The $^{13}C$ enhanced inner shell tubes exhibit dramatic advantages for $^{13}C$ NMR spectroscopy. Not only that the signal is enhanced by a factor of about ten, it is also highly selective and originates almost only from the latter. Any response from contaminating carbon phases is strongly suppressed. Figure 24, right panel has some demonstrations. The top spectrum in the figure displays the response for un-substituted SWCNTs together with the expected line shape resulting from the chemical shift anisotropy of the NMR g factor. The two lower spectra represent the static and the magic angle spinning response for the highly $^{13}C$ enriched inner tubes. Both lines are downshifted to about 111 ppm as compared to 124 ppm for the un-substituted tube, and also broadened. Both effects are at least partly due to high curvature. The downshift reflects the approach to a $sp^3$ hybridization for which the $^{13}C$ NMR resonance is know to appear at 65 ppm. A contribution of the shielding of the magnetic field due to the outer tubes can, however, may also contribute to the downshift. The

line shape for the response from the static NMR does not any more represent the chemical shift anisotropy. It is rather distorted from the distribution of small tube diameters which correlates to a distribution of $sp^2$ admixture. The same argument holds for the line broadening of the MAS response.

### 3.4. CLUSTERING OF MODES AND PAIR SPECTRA

The Raman response for the RBM from the inner tubes revealed too many lines which could partly be explained by the different density in the geometrically allowed inner and outer tubes. To take care for the large number of tubes, however, also combinations of inner – outer pairs with not optimized wall to wall distance must be considered. In addition, a comparison of the inner tube RBM spectra to the RBM response from HiPco tube in the same diameter range revealed a significant absence of lines in the latter material as compared to the signals from the inner shell tubes. This is demonstrated in Fig. 23. In addition, the values obtained for $C_1$ and $C_2$ from the assignment procedure described above exhibited some discrepancies to a recent analysis of the RBM in HiPco tubes[17,33]. It was therefore desirable to get an complete frequency and cross section analysis for the RBM line of the inner tubes. Due to the small diameter of the inner tubes the tight binding derived relation between RBM frequency and optical transition energies (Kataura plot from Fig. 9 was expected to be

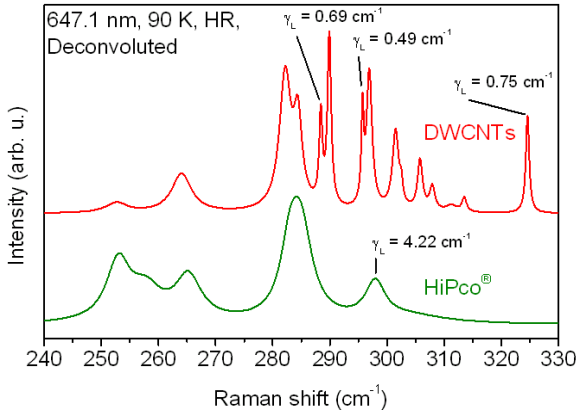


Fig. 23 Raman response for the RBM of the inner tubes (upper spectrum) as compared to the response from HiPco tubes (lower spectrum).

insufficient for this purpose, since it does not include curvature effects. Instead, it turned out that extended tight binding calculations using symmetry adapted non orthogonal tight binding wave functions as reported by V. Popov[20] is a

better approach. It reveals dramatic differences to the simple tight binding calculation for tube diameters smaller than 1 nm. Results from such

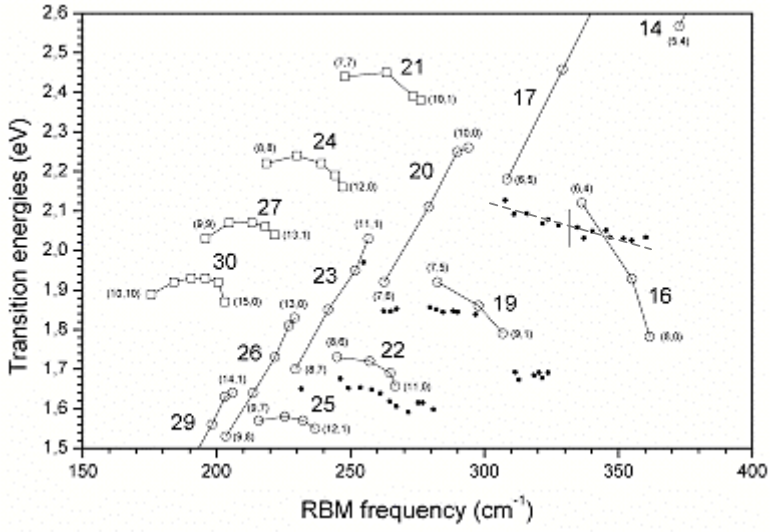


Fig. 24 Popov-Kataura plot for the relation between transition energy and RBM frequencies as obtained from an extended tight binding calculation and HiPco mateial. Open symbols: averaged for HiPco tubes[17,33] or calculated values. Lines: connect tubes from the same family with family number indicated. Full symbols: observed values for the peak resonance of the inner tubes.

calculations are depicted in Fig. 24 in comparison to results from HiPco tubes. Several striking information can be obtained.

1. The response from the inner tubes follows the same family behavior as the response from the HiPco tubes but the transition energy is generally downshifted by about 50 meV.
2. There is a considerable number of lines which exhibit the almost the same resonance transition energy even though the frequencies spread out as much as 30 $cm^{-1}$.
3. The number of lines in the cluster and thus the width of the cluster increases with decreasing tube diameter.
4. The low frequency end of the clustered lines match well to the results from the calculation and to the experimental results from the HiPco tubes. Therefore the cluster can be assigned to one particular inner tube which has the right resonance energy. This effect is best seen for the (6,4) tube of family 16 and the (6,5) tube of family 17. These tubes have 14 members in the cluster as determined from a high resolution measurement at low temperatures (see also Fig. 25).

5. Within the cluster the resonance energies are slightly decreasing with increasing RBM frequency. The averaged value for the decrease is –2 meV/cm$^{-1}$ as indicated by the dashed line in the figure.

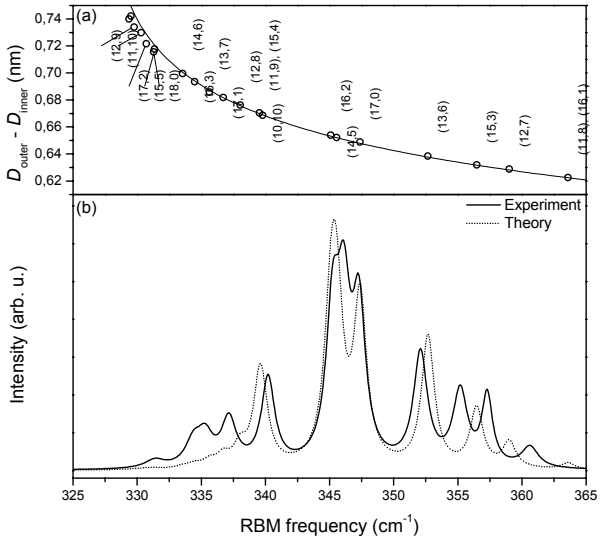


Fig. 25 Upper pannel: RBM frequencies (x-axis) versus difference in tube diameters (y-axis) as calculated for a (6,4) inner tube and various outer tubes. Lower pannel: composed spectrum as observed for the (6,4) cluster (full line) and calculated spectrum where the frequencies from the upper part of the figure were dressed with Lorentzian lines and the intensities were weighted by a Gaussian distribution.

The results can be interpreted in a sense that one inner tube can grow in many, up to 14, different outer tubes and the radial tube-tube interaction is responsible for the line shift. In other words the outer tubes implement a pressure on the inner tubes which causes the line shift. The line shift can
be calculated in a continuum model approximation where a van der Waals potential was assumed responsible for the tube-tube interaction and the dynamical matrix for the frequencies was solved explicitly under these conditions. Results of the calculation are depicted in the upper part of Fig. 25. The lower part of the figure has a composed spectrum where the strongest response for each component of the cluster was fit by a Voigtian line and the total of these line was composed to the spectrum shown in Fig. 25. In this way the spectrum directly represents the population of the pairs of the inner (6,4) tube and the various outer tubes in the cluster. The dotted spectrum was obtained by using the calculated frequencies and dressing them with Lorentzian lines. Intensities were takan from an assumed Gaussian distribution.

In detail the logistic is a bit more complicated. During the growth process various inner tubes are able to grow in a given type of outer tube. This hold for a reasonably large number of outer tubes. Thus, the (6,4) tube exists in a large number of different outer tubes but there is also a large number (may be ten times more) of the same outer tubes which do not host a (6,4) tube. It is the process of photo-selective Raman scattering which singles out the various (6,4) pairs. In other words the very strong Raman response of the (6,4) tubes comes only from approximately one tenth of the tube pairs. This multiplies to with the factor of one third from the mass relation. Thus, eventually the strong Raman response from the inner tubes comes only from 1/30th of the tube material. The higher electron-phonon coupling and the longer lifetime of the excited state are probably the reason for this giant resonance Raman effect.

## 4. Summary

In summary we presented in this contributions some fundamental aspects of Raman scattering with particular emphasis on resonance excitation. A classical and a quantum-mechanical description is provided. Dispersion of Raman lines and Fano Breit-wigner interferences are discussed. In the second part of the manuscript an extensive description of Raman scattering from SWCNTs is given. The origin of quantum oscillation for the RBM, the amount of cross section enhancement and the diameter dependence of the graphitic mode are discussed. This part also contains a review on the Raman response to doping and on the peapod systems. Finally, in the last chapter the special topic of Raman scattering from the inner shell tubes in DWCNTs is summarized. These systems are special since the inner tubes have a high curvature and an extremely strong Raman effect. By substitution of the natural carbons of the inner tubes with $^{13}C$ carbons challenging effects in Raman line shifts and in NMR spectroscopy are reported.

## 5. Acknowledgements

Work supported by the FWF Nr. 17345 and EU BIN2-2001-00580 and MEIF-CT-2003-501099 projects. Discussions with V. Popov are acknowledged.

## References

1. M. Cardona, Light Scattering in Solids, *Topics in Applied Physics* Vol 8, (Springer, Berlin, Heidelberg, 1983)

2. H. Poulet , J.P. Mathieu, Vibrational Spectra and Symmetry of Crystals, (Gordon & Breach, Paris, 1970)
3. H. Kuzmany, Solid State Spectroscopy, (Springer, Berlin, Heidelberg 1999)
4. G. Turell, Infrared and Raman spectra of Crystals, (Academic, London, 1972).
5. D.A. Long, Raman Spectroscopy, (McGraw-Hill, New York 1977).
6. G. Abstreiter, in Light Scattering in Solids IV, M. Cardona, G. Güntherrodt (eds.) *Topics in Appl. Phys*. Vol 54 (Springer, Berlin, Heidelberg 1984).
7. M.L. Bansal, A.K. Sood, M. Cardona, *Solid State Commun*. 78, 579 (1991).
8. D. Olego, M. Cardona, *Phys. Rev. B* 23, 6592 (1981).
9. C. Thomsen and S. Reich, *Phys. Rev. Lett.* 85, 5214 (2000).
10. M. S. Dresselhaus, G. Dresselhaus, and Ph. Avouris, Carbon Nanotubes: Synthesis, Structure, Properties and Applications (Springer-Verlag, Berlin, 2001).
11. R. Saito, G. Dresselhaus, and M. S. Dresselhaus, Physical Properties of Carbon Nanotubes, Imperial College Press (London), 1998.
12. S. Reich, C. Thomsen, J. Maultsch, Carbon Nanotubes, (Wiley-VCH, Weinheim, 2004).
13. H. Kataura, Y. Kumazawa, Y. Maniwa, I. Umezu, S. Suzuki, Y. Ohtsuka, and Y. Achiba, *Synth. Met.* 103, 2555 (1999).
14. R. A. Jishi, L. Venkataraman, M. S. Dresselhaus, and G. Dresselhaus, *Phys. Rev. B* 51, 11176 (1995).
15. H. Kuzmany, W. Plank, M. Hulman, Ch. Kramberger, A. Grüneis, Th. Pichler, H. Peterlik, H. Kataura and Y. Achiba, *Eur. Phys. J. B* 22, 307 (2001).
16. A. Kukovecz, Ch. Kramberger, V. Georgakilas, M. Prato and H. Kuzmany, *Eur. Phys. J. B* 28, 223 (2002).
17. C. Fantini, A. Jorio, M. Souza, M. S. Strano, M. S. Dresselhaus, and M. A. Pimenta, Phys. Rev. Lett. 93, 147406 (2004).
18. A. Jorio, R. Saito, J. H. Hafner, C. M. Lieber, M. Hunter, T. McClure, G. Dresselhaus, and M. S. Dresselhaus, Phys. Rev. Lett. 86, 1118-1121 (2001)
19. A. Grüneis Diploma work , University of Vienna 2001.
20. V. N. Popov, New. J. Phys. 6, 17 (2004).
21. O. Dubay, G. Kresse, H. Kuzmany, *Phys. Rev. Lett*. 88, 235506 (2002).
22. R. Pfeiffer, unpublished.
23. J. L. Sauvajol, 2004, unpublished
24. H. Kuzmany, W. Plank, and M. Hulman, Adv. Sol. St. Phys. 40, 194 (2000).
25. B. W. Smith, M. Monthioux, and D. E. Luzzi, Nature 396, 323 (1998).
26. R. Pfeiffer, H. Kuzmany, T. Pichler, H. Kataura, Y. Achiba, M. Melle-Franco, and F. Zerbetto, Phys. Rev. B 69, 035404 (2004)
27. T. Pichler, H. Kuzmany, H. Kataura, and Y. Achiba, Phys. Rev. Lett. 87, 267401 (2001)
28. S. Pekker, G. Oszlanyi, G. Faigel, Chem. Phys. Lett. 282, 435 (1998).
29. B. W. Smith, and D. E. Luzzi, Chem. Phys. Lett. 321 169 (1999).
30. Ch. Kramberger, R. Pfeiffer, H. Kuzmany, V. Zólyomi, and J. Kürti, Phys. Rev. B 68, 235404 (2003).
31. R. Pfeiffer, H. Kuzmany, F. Simon, S. N. Bokova, and E. Obraztsova, Phys. Rev. B 71, 155409 (2005).
32. F. Simon, Ch. Kramberger, R. Pfeiffer, H. Kuzmany, V. Zólyomi, J. Kürti, P. M. Singer, and H. Alloul, Phys. Rev. Lett. 95, 017401 (2005).
33. H. Telg, J. Maultzsch, S. Reich, F. Hennrich, C. Thomsen, Phys. Rev. Lett. 93, 177401 (2004).